Received: 7 September 2022 | Revised: 19 August 2022 | Accepted: 7 September 2022

DOI: 10.1002/mp.16005

RESEARCH ARTICLE

MEDICAL PHYSICS

3D-printed large-area focused grid for scatter reduction in cone-beam CT

Santiago Fabian Cobos[1] | **Christopher James Norley**[2] | **Hristo Nikolaev Nikolov**[2] | **David Wayne Holdsworth**[1,2]

[1]Department of Medical Biophysics, Western University, London, Ontario, Canada

[2]Robarts Research Institute, Western University, London, Ontario, Canada

Correspondence
Dr. David Holdsworth, Robarts Research Institute, Western University, London, Ontario N6A 3K7, Canada.
Email: dholdsworth@robarts.ca

Funding information
Canadian Institutes of Health Research, Grant/Award Number: FDN 148474; Ontario Research Fund, Grant/Award Number: RE-077-66

Abstract

Background: Cone-beam computed tomography (CBCT) systems acquire volumetric data more efficiently than fan-beam or multislice CT, particularly when the anatomy of interest resides within the axial field-of-view of the detector and data can be acquired in one rotation. For such systems, scattered radiation remains a source of image quality degradation leading to increased noise, image artifacts, and CT number inaccuracies.

Purpose: Recent advances in metal additive manufacturing allow the production of highly focused antiscatter grids (2D-ASGs) that can be used to reduce scatter intensity, while preserving primary radiation transmission. We present the first implementation of a large-area, 2D-ASG for flat-panel CBCT, including grid-line artifact removal and related improvements in image quality.

Methods: A 245 × 194 × 10 mm 2D-ASG was manufactured from chrome–cobalt alloy using laser powder-bed fusion (LPBF) (AM-400; Renishaw plc, New Mills Wotton-under-Edge, UK). The 2D-ASG had a square profile with a pitch of 9.09 lines/cm and 10:1 grid-ratio. The nominal 0.1 mm grid septa were focused to a 732 mm x-ray source to optimize primary x-ray transmission and reduce grid-line shadowing at the detector. Powder-bed fusion ensured the structural stability of the ASG with no need for additional interseptal support. The 2D-ASG was coupled to a 0.139-mm element pitch flat-panel detector (DRX 3543, Carestream Health) and proper alignment was confirmed by consistent grid-line shadow thickness across the whole detector array. A 154-mm diameter CBCT image-quality-assurance phantom was imaged using a rotary stage and a ceiling-mounted, x-ray unit (Proteus XR/a, GE Medical Systems, 80kVp, 0.5mAs). Grid-line artifacts were removed using a combination of exposure-dependent gain correction and spatial-frequency, Fourier filtering. Projections were reconstructed using a Parker-weighted, FDK algorithm and voxels were spatially averaged to 357 × 357 × 595 μm to improve the signal-to-noise characteristics of the CBCT reconstruction. Finally, in order to compare image quality with and without scatter, the phantom was scanned again under the same CBCT conditions but with no 2D-ASG. No additional antiscatter (i.e., air-gap, bowtie filtration) strategies were used to evaluate the effects in image quality caused by the 2D-ASG alone.

Results: The large-area, 2D-ASG prototype was successfully designed and manufactured using LPBF. CBCT image-quality improvements using the 2D-ASG included: an overall 14.5% CNR increase across the volume; up to 48.8% CNR increase for low-contrast inserts inside the contrast plate of the QA phantom; and a 65% reduction of cupping artifact in axial profiles of water-filled cross sections of the phantom. Advanced image processing strategies to remove grid

line artifacts did not affect the spatial resolution or geometric accuracy of the system.

Conclusions: LPBF can be used to manufacture highly efficient, 2D-focused ASGs that can be easily coupled to clinical, flat-panel detectors. The implementation of ASGs in CBCT leads to reduced scatter-related artifacts, improved CT number accuracy, and enhanced CNR with no increased equivalent dose to the patient. Further improvements to image quality might be achieved with a combination of scatter-correction algorithms and iterative-reconstruction strategies. Finally, clinical applications where other scatter removal strategies are unfeasible might now achieve superior soft-tissue visualization and quantitative capabilities.

KEYWORDS
additive manufacturing, antiscatter grid, computer tomography, cone-beam CT, laser melting, parametric modeling, scatter, selective, 3D printing

1 | INTRODUCTION

Cone-beam computed tomography (CBCT) emerged during the late 1990s as a volumetric, high-resolution, low-dose, imaging tool, ideally suited for guided radiation therapy, cranial angiography, and maxillofacial radiology.[1–3] Currently, CBCT is increasingly supplanting traditional CT modalities in many clinical applications, such as respiratory or cardiac imaging. Compared to traditional CT, CBCT maintains and improves spatial resolution while reducing costs, scanning times, and patient dose.[4–7] However, the large field-of-view of CBCT geometries leads to increased detected scatter fraction (i.e., 0.05–0.15, for fan-beam and spiral CT, vs. 0.4–2.0 for CBCT), which degrades image quality, especially in high scatter-to-primary (SPR) scenarios.[8–11] Scatter contamination of the projection images results in tomographic reconstructions with reduced contrast-to-noise ratio (CNR), worsened CT number inaccuracies, and increased shading artifacts.[12–16] Clinically, scatter-induced image artifacts and nonlinearities translate into limited soft-tissue visualization,[17,18] reduced efficacy of image-guided interventions,[19,20] incompatibility with quantitative analysis,[14,21] and can lead to an inaccurate diagnosis or misdiagnosis.[22,23]

Therefore, it is essential to include scatter-ameliorating strategies into CBCT system design, without increasing patient dose. In general, scatter-reduction strategies can be divided into two approaches: (1) hardware techniques to reject scatter and (2) software techniques to correct scatter.[21,24,25] In practice, hardware techniques do not completely suppress the scatter reaching the detector and, similarly, no software methods correct artifacts perfectly. For these reasons, an optimal scatter correction is likely to combine both hardware and software approaches.[26] Hardware methods such as the air-gap technique, bowtie filters, or antiscatter grids reduce the number of scattered x-rays reaching the detector.[27] Software methods derive or estimate the scatter field using models based on physical, empirical, or consistency criteria to correct the acquired projection data.[28] The major drawbacks of software-based methods are related to their computational intensity, which might prevent real-time applications. Additionally, they often require a priori knowledge of the material and density distributions of the object—requiring additional radiation dose.[27–29] Model-based scatter correction methods, software-based methods, which do not require additional dose, have recently shown to provide improvements in CT number accuracy and scatter-related artifact reduction.[27,28] Nonetheless, these methods may not reach the levels of scatter correction required for quantitative applications.[30] In contrast, hardware methods do not require a priori knowledge about the object, but cannot always be implemented due to space restrictions (e.g., air gap) or require additional radiation dose to account for primary x-ray intensity loss (e.g., traditional antiscatter grids with interseptal spacers).[24,27,29,31,32] Furthermore, failure to correct artifacts introduced by a grid can compromise the potential improvements in image quality.[33,34] However, a new generation of metal, 3D-printed, antiscatter grids, which are the focus of this manuscript, offer a promising solution for hardware-based scatter rejection in CBCT.[24,35]

Antiscatter grids are mechanical devices that are placed directly in front of the x-ray detector to capture scattered photons while preserving primary x-rays.[24,35–38] Traditionally, these grids have been manufactured using a one-dimensional array of thin (approximately 15–46 μm) lead septa supported by aluminum or fiber spacers.[39,40] As previously mentioned, the interseptal support material has the disadvantage of attenuating primary x-rays that might subject the patient to a higher radiation dose to maintain image quality.[27,41] Even using sophisticated fabrication methods like the ones described by Lehmann et al.[42] and Goldenberg et al.,[43] this limitation cannot be overcome. Recent

advancements in additive manufacturing (AM) and laser, powder-bed fusion (LPBF) allow the fabrication of novel, two-dimensional focused grids (2D-ASGs) that do not require interseptal support.[24,33,35] This 3D structures are built by selective melting of metal powder, deposited in layers, using a high-energy, power-density laser.[44–46] 2D-ASGs provide improved scatter-removal characteristics over 1D-ASGs, and increase primary transmission up to as much as 70% of the incident x-ray beam.[24] These novel grids achieve this additional transmission by focusing the grid septa toward the x-ray source focal spot and inherently eliminate geometrical distortion of the grid shadow across the detector.[24,38,39]

2D-ASGs prototypes have been shown to improve image contrast and reduce scatter-related artifacts for CBCT systems.[24,35] However, uncertainties persist with regard to the impact that grid septa might have on the projection data. For instance, detector elements covered by grid septa receive a reduced count of x-ray photons (i.e., x-ray fluence), leading to grid-line artifacts (GLAs). Furthermore, signal leaking from the surrounding, non-affected elements causes exposure-dependent gain variations. The combination of both effects—reduced fluence and signal leakage—renders conventional pixel-to-pixel variation correction methods ineffective.[47,48] In such a case, the CBCT reconstruction can be affected by severe ring artifacts that impair radiological interpretation and analysis.[33,47] Another limitation of recently investigated 2D-ASG prototypes relates to their coverage area of the detector. Although the 3D printing of focused, antiscatter grids for scatter rejection is available as a commercial service,[49] to our knowledge, there is no report in the literature for the design and evaluation of a highly focused antiscatter grid covering a significant area of a flat-panel detector in a full-beam CBCT geometry. The largest 2D-ASG prototype manufactured commercially and described in the literature for a half-beam CBCT geometry is limited to a grid of size 20 × 3 cm.[33] Furthermore, it remains unclear how residual stresses, which are characteristic of LPBF, might affect the fabrication of large-area grids (e.g., build failure due to object-substrate delamination) or during subsequent clinical use (e.g., geometric distortion or crack formation).[44,50]

We present the complete process of design, manufacturing, and implementation of a large area, 24.5 × 19.4 cm, focused 2D-ASG, and evaluate its quantitative effects in CBCT image quality. We first developed an open-source, parametric modeling module to generate a focused-grid, computer-aided design (CAD). Based on this CAD model, we optimized the 3D printing parameters of a commercially available laser powder-bed fusion system to achieve geometric stability and thin septa in the grid. Using clinically available equipment, we acquired CBCT data of a quality assurance phantom, and assess image quality with and without the antiscatter device. Finally, we describe the image processing techniques required to successfully correct GLAs and describe the improvements in CBCT image CNR, CT number accuracy, and shading artifacts. Our results show that two-dimensional, focused, 3D-printed, metal grids provide an effective solution for scatter rejection in large-area CBCT.

2 | METHODS

2.1 | 2D antiscatter grid parametric modeling

The computational power required to create and manipulate CAD files is directly related to the number of vertices of the 3D model.[51] Large-area 2D-ASGs require many unique cells, because each cell is oriented at a unique angle along a ray between the focal spot of the x-ray source and each point on the detector. This unique angular orientation makes it impossible to simply replicate a single septal cell as a unit cell. A minimum of 12 vertices is required to define each septal cell of the 2D-ASG. Our large-area grid has 219 × 172 septal cells, requiring close to half a million vertices in the CAD file. Conventional CAD modeling packages and methods typically require at least an order of magnitude more than the minimum number of vertices to define the geometry sufficiently for Boolean operations. Even if the fourfold symmetry of this grid were exploited to reduce the number of vertices, this number remains computationally unwieldy.[52] Additionally, this division of the geometry into quadrants requires the extra step of geometric transformations and stitching them together into a final assembly. Figure 1 shows a diagram of the basic geometry and features of the novel grid design.

Changing any geometric parameter of the grid will require recalculation and regeneration of a completely new drawing of the CAD model. Redrawing of the grid may be necessary to accommodate changes in x-ray detector dimensions, detector element pitch, and source-to-detector distance of the CBCT system, among other design constraints. To circumvent the computational power and modeling time challenges inherent in using conventional 3D modeling packages,[52] we have designed and implemented a parametric modeling node-tree technique. This was achieved using a Python-based solution in the open-source software (Blender 2.8). The node-tree required seven user-defined parameters (Table 1) to generate an optimized stereolithographic file (STL) compatible with a commercial LPBF printing interface (QuantAM, Renishaw).

Despite the advantages of the parametric tool being able to generate grids with any combination of parameters, limitations of the design are mandated by the AM process, described below. For instance, the size of the grid frame cannot exceed the limits of the build plate of the LPBF machine. Fine-tuning of the laser scan time is

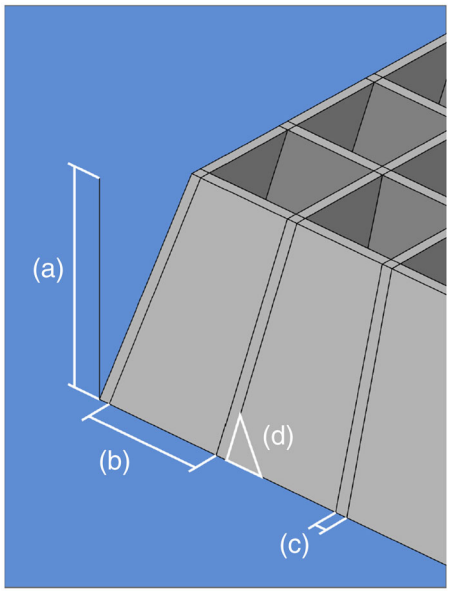

FIGURE 1 Close-up of 2D-ASG septal cell. (a) Grid height, (b) element size, (c) septal thickness, and (d) inclination angle to match CBCT geometry

TABLE 1 2D-ASG design parameters

Parametric modeling inputs	2D-ASG design parameters
Frame length	245 mm
Frame width	194 mm
Cell aperture size	1 mm
Septal thickness	0.1 mm
Frame height	10 mm
Build-plate clearance	1 mm
Focal spot distance	732 mm

required for various combinations of powder particles and laser spot size to attain mechanically stable thin septa.[53] In our implementation, particle size and scanning time, limited septal thickness to ~100 μm, and frame size to 250 × 200 mm (Figure 2). Prior to 3D printing, mounting flanges and a label were added to the grid frame to aid with installation and identification of the device.

2.2 | 2D-ASG manufacturing

The parameters used to design our large-area grid are defined in Table 1. Additionally, the 2D-ASG had a grid-ratio of 10:1, a pitch of 0.909 lp/mm, and a rectangular array of 219 × 172 square elements. Grid ratio is defined as the ratio of the height of the grid septa to the distance between them. The 2D-ASG was manufactured using a commercially available LPBF 3D printer (AM-400; Renishaw plc, New Mills Wotton-0-under-Edge, UK) in

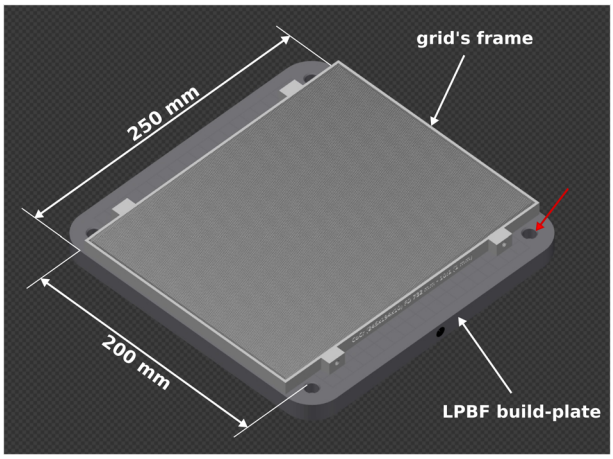

FIGURE 2 QuantAM 3D printing interface preview of grid placement in the (250 × 250 mm) build plate. Red arrow shows build-plate securing clearance holes, which limited grid size in one dimension.

277 layers, each 40 μm in thickness, using cobalt–chrome metal-alloy powder (60–65% Co, 25–35% Cr, and 3–7% Mo) 15–45 μm in diameter. The cobalt–chrome alloy was used due to its widespread usage in the LPBF industry and sufficiently high x-ray attenuation at relatively low energies (i.e., 30 cm^{-1} at 42.4 keV).[54–56] Although tungsten has been commonly reported as the material of choice for 2D-ASG manufacturing,[33,35,38] our goal was to evaluate the performance of a large-area 2D-ASG prototype using a readily available alloy. In the additive-manufacturing facility at our institution (ADEISS), cobalt–chrome is routinely used for the production of customized medical parts. Furthermore, due to the high melting point and high thermal conductivity of tungsten, the LPBF process for that material requires higher energy output,[54,57] which makes tungsten 2D-ASGs less accessible and more expensive.[45] Finally, our cobalt–chrome 2D-ASG was designed to be used for clinical cases where energies up to 80 kVp are used (e.g., for peripheral cone-beam CT scanning); we do not anticipate cobalt–chrome to perform better than other metals (e.g., tungsten or lead) when higher energies are required.

Prior to building the full-size 2D-ASG, several smaller prototypes were manufactured to optimize the LPBF printing parameters. Thin septa were achieved using a "single-path" strategy (Figure 3b) where the ytterbium-fiber laser, operating at 100 W, employed a longer-than-usual (60 μs) dwell time and traversed each cell septa a minimum number of passes to achieve the desired thickness. Despite using a 70-μm diameter laser focal spot size, this scanning strategy produced nominal 100 μm walls due to expansion of the melting pool and the adhesion of surrounding powder, the latter of which is the main cause of surface roughness in LPBF.[58] To maintain the desired septal thickness and still ensure structurally stable septa, the distance between two

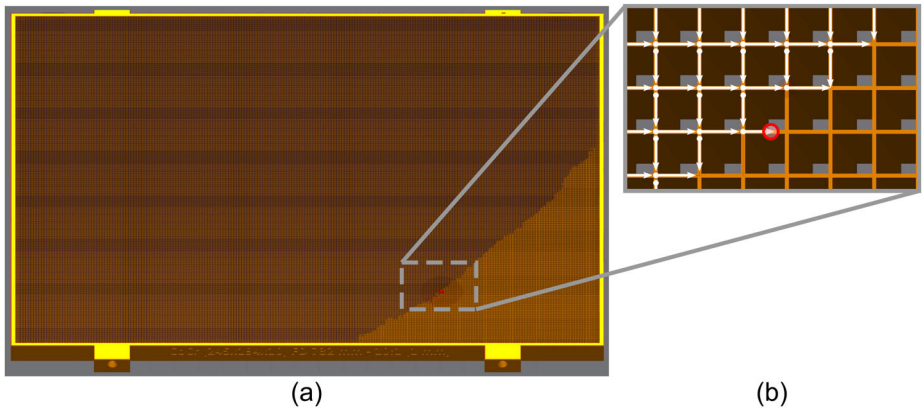

FIGURE 3 QuantAM laser scanning strategy preview for the top layer of the large-area, focused, 2D-ASG. (a) Laser scanning pattern starting at the top-left corner of the grid's frame. (b) Close-up of grid septa being consolidated with a single laser path, white arrows show the progression of laser position across the grid.

consecutive points when the laser was on was set to 60 μm. The laser scanning pattern across the grid frame was determined automatically by QuantAM software. The pattern had a radial configuration starting at the top-left corner of the grid frame (Figure 3a).

Rapid, repeated, heating, and cooling cycles, which are characteristic of LPBF, are responsible for high residual stress build-up in the 3D-printed part.[50,59] The laser scanning pattern and the inherent heat-dissipating nature of the grid geometry helped minimize thermal stress during printing. After LPBF was completed, the operator removed the nonconsolidated powder, and the grid was heat-treated in an argon-atmosphere oven to relieve any residual stresses. The oven set temperatures, 450°C and 750°C, were ramped up gradually over 60 min. Each temperature was maintained for 45 min with no cooling time between cycles. The oven temperature was reduced gradually at the end of the cycle allowing the part to cool down naturally.

Wired electrical discharge machining (wire-EDM) was used to carefully detach the large area, focused, 2D-ASG from the build plate. The designed grid ratio of 10:1 was maintained thanks to the included 1-mm build-plate clearance (Table 1). The 2D-ASG exhibited strength and stability without additional interseptal supports, and sustained no damage during regular manipulation.

2.3 | Verification of grid septa dimensions

The 2D-ASG was inspected for dimensional accuracy and build quality using an image-based technique employing a measuring microscope (STM6, Olympus). The grid was placed on the bed of the measuring microscope and oriented perpendicular to the microscope image plane by maximizing observed pixel intensity. This was repeated over five different locations—center and peripheral edges—across the face of the 2D-ASG. The grid septa were oriented orthogonal to the image matrix of the microscope to facilitate pixel counting. Regions of interest (ROIs) circumscribing the septal wall and a small region outside the wall, and excluding the septal intersections were selected and cropped. Each ROI was thresholded at the full-width-half-max (FWHM) of the intensity values to create binary images. The number of pixels across each line of the binary images, perpendicular to the septal wall, was counted and mean and standard deviation values were calculated. This technique ensures that the width of the septal wall is accurately and precisely assessed over its entire length and in all sections of the grid unit.

2.4 | CBCT experimental setup

Cone-beam systems have, generally speaking, two different architectures. Stationary-object systems require the x-ray source and detector to be mounted on a gantry that is rotated around the object. With a stationary-source system, the object rotates in the path of the x-ray beam—often employed for small, bench-top systems. Our stationary-source design (Figure 4) consisted of a ceiling-mounted x-ray source (Proteus XR/a, GE Medical Systems) placed 732 mm away from a commercially available 383.5 × 459.5 × 14.7 mm, flat-panel detector with 139 μm element pitch (DRX 3543, Carestream Health). A computer-controlled, precision stage (Model PSR300, Intellidrives) was used to obtain 215 projections at one-degree angular increments for each Parker-weighted CBCT reconstruction in this study. Alignment of the detector was achieved by minimizing the width of the shadows cast by the septa of the grid on the detector. When the detector was properly aligned, the width of the septa shadows appeared both minimized and uniform across the face of the 2D-ASG.

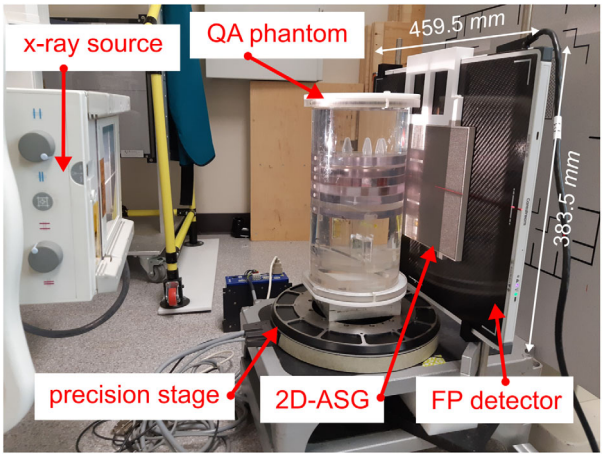

FIGURE 4 Custom, stationary-source, CBCT experimental setup. Ceiling-mounted x-ray unit, precision rotary stage, 2D-ASG, and flat-panel digital detector

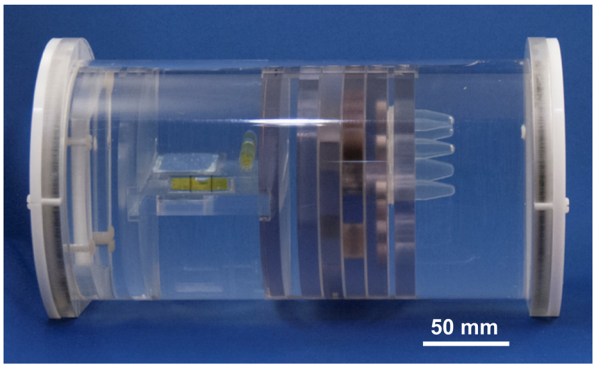

FIGURE 5 (305 × 154 mm) modular QA phantom used to evaluate CBCT image quality characteristics. The different sections and plates are arranged from left-to-right in the image.

CT data of a water-filled, quality assurance phantom (Figure 5) was acquired, with and without the grid, at 80 kVp and 0.5 mAs to evaluate the performance of the 2D-ASG. No other scatter-rejecting techniques were implemented to assess the effects of 2D-ASG alone. The 2D-ASG was placed directly in front of the detector using a custom 3D-printed clip, and primary transmission was evaluated using a primary transmission map,[24] T(x, y), using:

$$T(x,y) = \frac{I_{grid}}{I_{no-grid}}, \quad (1)$$

where I_{grid} is the pixel intensity value with no grid present and $I_{no\text{-}grid}$ the mean intensity of the same pixel with the 2D-ASG in place. To evaluate the geometric stability of the CBCT system, high-contrast, radio-opaque, 1 mm beads were attached to the QA phantom and a CT data set was acquired. As the phantom was rotated, the beads were expected to trace a sinusoidal path allowing the detection of geometric deviations. The mean deviation of beads from a best-fit sinusoid for each projection image was used to correct the phantom data prior to CBCT reconstruction.[60]

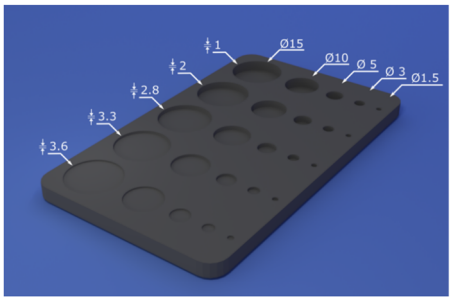

FIGURE 6 3D rendering of the design of the 2D, 3D-printed, low-contrast phantom

2.5 | 2D low-contrast visualization

In plain 2D projections, scatter significantly reduces low-contrast object visualization.[11,24] We evaluated the effectiveness of the 2D-ASG to mitigate the reduction in CNR by acquiring 2D-projection radiographs of a plastic, 3D-printed, low-contrast phantom (Figure 6). The phantom was radiographed with and without the 2D-ASG and in the presence of a 15-cm water bath acting as a scatter source. The low-contrast phantom consisted of 25 cylindrical holes of various diameters and depths. Contrast-to-noise was calculated using the following.

$$CNR = \frac{|C-B|}{\frac{1}{2}(\sigma_C+\sigma_B)}, \quad (2)$$

where C is the signal value of the low-contrast object and B the signal value of the object background, σ_C and σ_B, are their respective standard deviations.[24]

2.6 | Grid-line artifact corrections and CBCT reconstruction

A limitation of the application of antiscatter grids in digital radiography is the reduced x-ray fluence at detector elements obscured by grid septa. This reduced fluence results in a reduced detected signal creating grid-line artifacts (GLAs) in the image.[27,33] In theory, if the area of the element obscured by the grid septa is small, then flat-field corrections should be able to reduce or remove these artifacts from the image. Conversely, if the area of the element covered by the grid is too large, this correction is unfeasible due to the low signal-to-noise ratio. For two-dimensional grids, this phenomenon can be further exacerbated in areas where the grid septa intersect. In our implementation, the detector elements were 139 × 139 μm, and the nominal grid-septa thickness was

100 μm. It is important to note that the detected signal intensity did not drop below 30% of the incident x-ray fluence in any of the detector elements; this is to be expected because the nominal septal thickness was designed to be less than the detector element size. Below, we describe a two-step method for GLA correction using a modified, exposure-dependent, flat-field correction[48] and a customized spatial frequency Fourier filter.

Flat-field correction is regularly used to account for pixel-to-pixel variations (i.e., fixed-pattern noise) in digital x-ray detectors. This strategy is able to successfully correct intensity variations for pixels unaffected by grid septa. However, it is ineffective for pixels that are partially obscured by grid septa due to exposure-dependent gain variations in these affected pixels. We have previously described the necessity to characterize exposure-dependent, pixel-to-pixel, gain variations by performing flat-field corrections at various exposure levels.[61] This correction was achieved using an adapted approach from Altunbas et al.[48] where we used six exposure levels (E)—achieved using copper filtration of the x-ray beam (0, 0.5, 1, 1.5, 2, and 2.5 mm thicknesses) to generate exposure-dependent (E) gain correction map, $G(x, y, E)$, for each exposure level that was calculated using the following:

$$G(x, y, E) = \frac{I^f_{no-grid}(x,y,E)}{I^f_{grid}(x,y,E)}, \quad (3)$$

where $I^f_{no-grid}(x, y, E)$ is the intensity value measured in analog to digital units (ADUs) of a flat-field image with no-ASG, and $I^f_{grid}(x, y, E)$ is the measured flat-field corrected pixel ADU with ASG. Data were organized using a multidimensional array (3072 × 2560 × 6), and pixel specific gain-factors were analyzed. Figure 7 shows the exposure-dependent variations in gain factors for a subset of pixels: representing pixels unaffected by grid artifacts, affected by grid septa, and affected by grid intersections.

Gain factors for pixels unaffected by grid artifacts remained at unity (i.e., standard deviations < 0.05), whereas pixels affected by grid artifacts were well described by a power function, $(ADU) = a \times ADU^b + c$. For such cases, curve coefficients (a, b, and c) were calculated (MATLAB, The MathWorks, Natick) and stored in a lookup table to reduce the computational burden of the correction. Projection images were corrected using this pixel-specific, exposure-dependent, gain correction.

In spite of the careful characterization of the gain response of detector elements obscured by the grid, faint grid-line artifacts remained visible in the projection data. However, the periodic nature of the grid-line artifacts allows implementation of a customized, fast-Fourier transform (FFT), notch filter to further reduce grid-line artifacts.[62] Only gridlines were affected by the

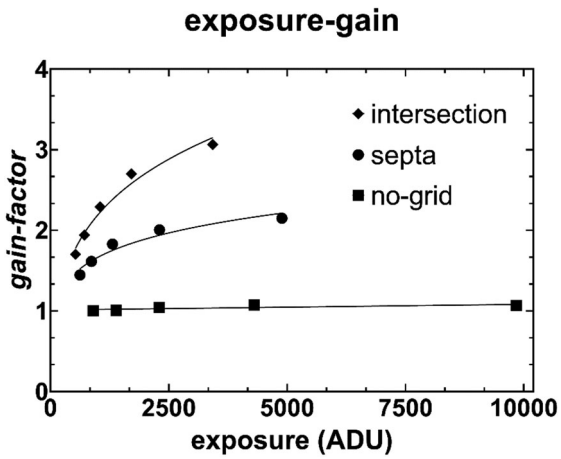

FIGURE 7 Exposure-dependent gain-factor variations for three, example, detector elements illustrating the effect of varying the degree of grid septa shadow. Septa represents pixels affected by a lower degree of shadowing and septa intersection represents pixels affected by a greater degree of shadowing. Power series curve fits are shown in solid lines.

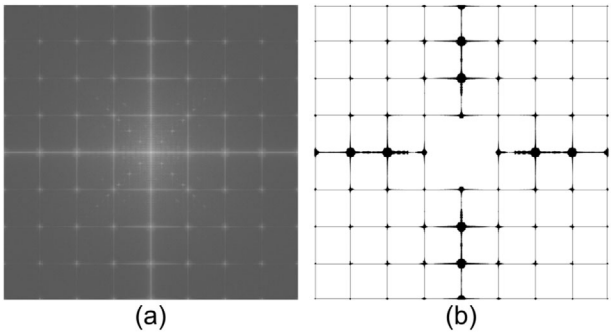

FIGURE 8 FFT images of an open acquisition with the 2D antiscatter grid in place. (a) FFT power spectrum. (b) Thresholded and manually segmented binary mask of FFT notch filter use to remove grid-line artifacts from projection images in frequency space

FFT filter because no other structures presented the same spatial frequency in the projection image data. Figure 8a shows the Fourier power spectrum of an open image with the grid in place. A binary mask was created using a combination of thresholding and manual segmentation of the power spectrum. This binary mask shown in Figure 8b was used to remove the selected frequencies of each projection image in frequency space.

The two sets of 215 projection images for each volume, with and without the 2D-ASG, respectively, were used to reconstruct CBCT volumes using a Parker-weighted FDK algorithm. The full-resolution volumes (119 × 119 × 119 μm) were spatially averaged to 357 × 357 × 595 μm, which is a clinically relevant voxel size,[63] to improve the signal-to-noise characteristics of the data. All CBCT-reconstructed volumes were scaled to consistent Hounsfield units (HUs) and all figures

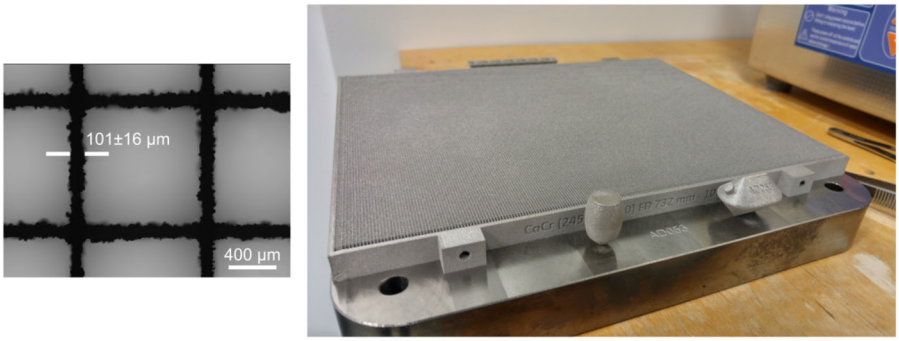

FIGURE 9 Large-area, focused, 2D-ASG after manufacturing and postprocessing. (a) Close-up of grid septa using the measuring microscope (nominal septal width was 101 µm). (b) Picture of the 2D-ASG after heat treatment still attached to the LBPF build plate

depicting comparisons between volumes are displayed using the same window and level values.

2.7 | CBCT data analysis

Quality assurance (QA) phantoms are an effective tool to accurately and precisely evaluate the performance of clinical CT systems qualitatively and quantitatively.[64,65] The phantom used in this study consisted of eight separated modular sections designed to assess the following aspects of CBCT image quality: spatial resolution, geometric accuracy, uniformity, noise, artifact characterization, CNR, and linearity. The technical details of the QA phantom can be found in Figure S1 in the Supporting Information for this manuscript.

Spatial resolution and geometric accuracy, evaluated by Sections 1, 2, 4, and 5 of the QA phantom, were used to determine overall image quality differences between the two CBCT reconstructions—with and without 2D-ASG. Spatial resolution was qualitatively assessed by calculating the modulation transfer function (MTF) using the two, slanted edges located in Sections 1 and 4.[64] Qualitatively, spatial resolution was also evaluated using the nine bar patterns (0.4–2.0 lp.mm^{-1}) of Section 5. Geometric accuracy of the system was measured using the embedded array of five 0.8 mm diameter steel beads (Section 2). Beads were arranged in a rectangular, 40×40 mm^2, pattern with one bead located exactly at the centroid.

Other sections of the phantom (3, 6, 7, and 8) were used to quantify improvements in image quality related to scatter rejection. The linearity plate of the QA phantom, which consists of 1.73 × 3.93 cm vials filled with various concentrations of iodine (15, 7.5, 3.75, 1.875, 0.9375, and 0 mg·mL^{-1}), was used to evaluate improvements in low-contrast visualization. CNR was calculated for each concentration of iodine using the same methodology described in the 2D low-contrast visualization section of this manuscript.

Shading artifacts (i.e., cupping and streaking) were evaluated using the water-filled uniformity and artifact characterization sections of the phantom, respectively. Cupping was quantitatively measured using the uniformity index (UI) within cylindrical ROI in Section 3 near the central reconstruction slice:

$$UI = \frac{I_{periphery} - I_{center}}{I_{center}}, \quad (4)$$

where $I_{periphery}$ and I_{center} are the mean intensities of ROIs located correspondingly. Qualitatively, cupping was visualized using radial signal profiles across the diameter of the uniformity section of the phantom. Finally, qualitative improvements in streak-artifact intensity were assessed by using the leaded-plastic inserts located in Section 6.

3 | RESULTS

3.1 | Parametric modeling

The Python-based node-tree parametric modeling tool was successfully created. The interface included a preview of the CAD design that updated every time a parameter was modified. The design of the 2D-ASG CAD file took less than 6 min following input of all the parameters.

3.2 | 2D-ASG postmanufacturing evaluation

Images of the 245 × 194 × 10 mm 2D-ASG after heat-treatment and before wire-EDM are shown in Figure 9, demonstrating mechanical stability and appropriate grid septa thickness (101 ± 16 µm). After wire-EDM, consistent grid height allowed the 2D-ASG to lay flat against the x-ray detector, which made grid-detector coupling straightforward to achieve. Mechanical

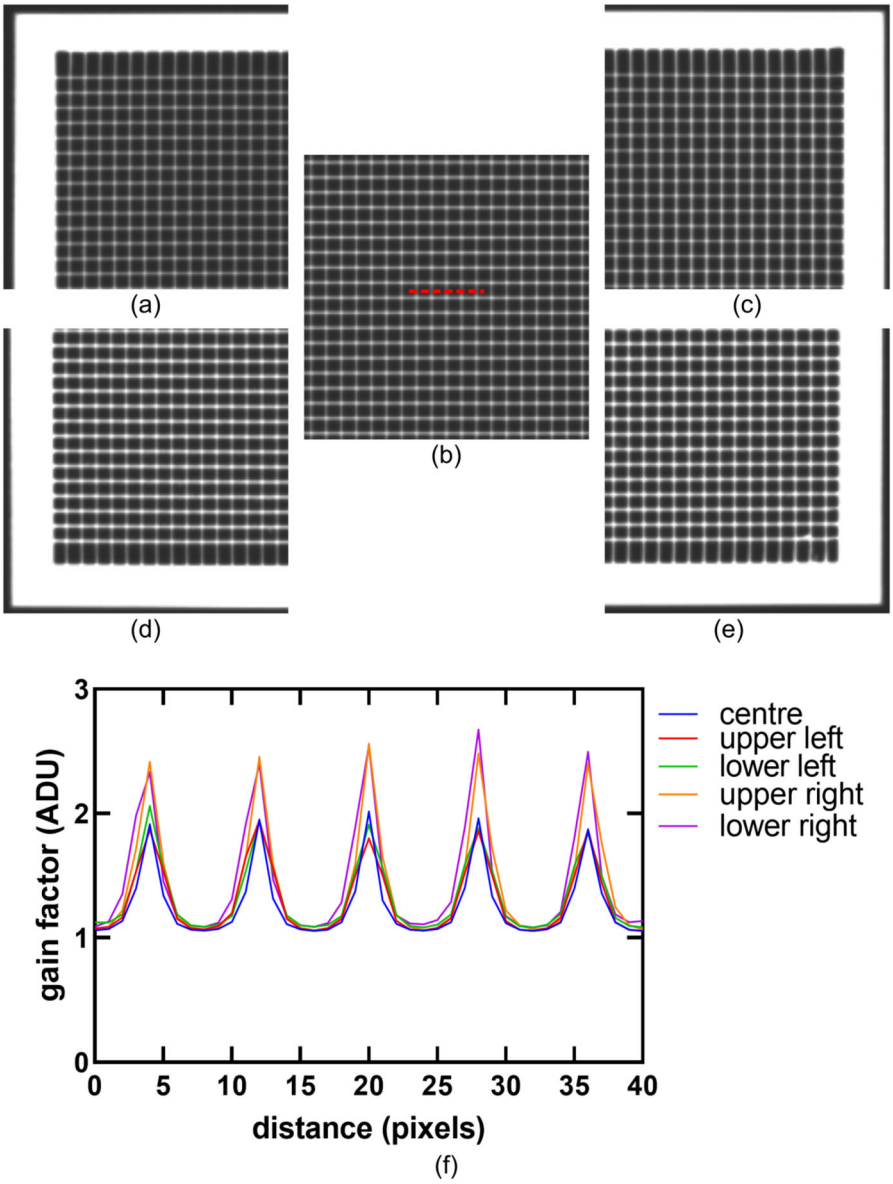

FIGURE 10 Grid-septa shadow consistency across the 2D-ASG (a–e) close-up images of gain maps at various regions of the grid upper left, center, upper right, lower left, and lower right, respectively. (F) Line profiles across five grid septa at each location showing consistency of grid-septa shadow thickness. The line profiles, for each region, were placed approximately in the same relative location marked by the red-dotted line in (b).

stability facilitated routine handling of the device as well as consistent grid shadows across the detector. Figure 10 shows close-up gain maps in different regions of the detector.

An average transmission of 78% was achieved, which is consistent with the nominal 101 μm, septa (Figure 9a). Since each 139 × 139 μm detector element might be covered by varying amounts of 2D-ASG septa, primary transmission is better depicted using a cumulative histogram of the transmission map (Figure 11). Detector elements located underneath grid–septa intersections received the lowest amount of primary transmission, ~30 %, whereas elements located in open grid channels received the largest amount of transmission, ~97%.

3.3 | 2D low-contrast visualization

Low-contrast object conspicuity (i.e., improved detection of small, low-contrast objects) is improved by a decrease in image noise. Figure 12a,b shows a side-by-side comparison of the 3D-printed, low-contrast phantom imaged without and with the 2D-ASG as described previously. CNR values, as a function of phantom's hole diameter and thickness, were improved for all cases.

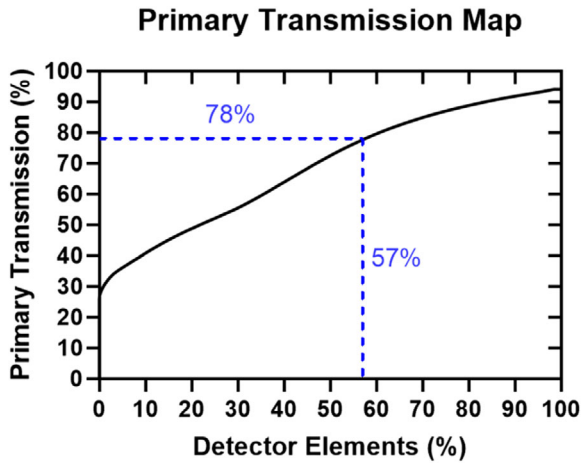

FIGURE 11 Cumulative histogram of the transmission map for a flood-field image of the large-area, focused, 2D-ASG. More than half (57%) of the detector elements exhibit transmission that is below the average value for the grid (78%).

Proportionally larger improvements were observed as the hole diameter decreased (Figure 12c,d).

3.4 | Evaluation of grid-line artifact correction

3.4.1 | In 2D projection images

Grid lines appear as vertical and horizontal lines with reduced x-ray fluence in raw 2D-projections (Figure 13a). Conventional gain correction tends to overcorrect grid-line artifacts because it does not take into account potential signal leaking from high-intensity neighbor detector elements. Figure 13b displays poorly corrected grid-line artifacts, where image intensity has been overcorrected. The proposed exposure-dependent gain correction strategy was able to reduce grid-line artifacts by >90% in high x-ray fluence regions of the image, and >60% in regions with low x-ray fluence (Figure 13c,d). The improved gain correction allowed satisfactory grid-line removal with the addition of a customized notch-FFT-filter.

3.4.2 | In CBCT reconstructions

Traditional linear-gain correction produced severe ring artifacts (i.e., s = 894.02 HU) when compared to the exposure-dependent gain correction (i.e., s = 85.55 HU) for homogeneous regions of the QA phantom. Exposure-dependent gain correction followed by Fourier-notch filtering improved the CT number precision by a further 31 HU. Qualitative analysis of line pairs showed appropriate maintenance of image spatial resolution (Figure 14).

Improvements in CT number accuracy for homogeneous materials were observed by analyzing HU variations across an air-filled slanted edge chamber inside the QA phantom. Ring artifacts caused by GLA were significantly minimized and residual rings were removed by Fourier filtering. Figure 15b,c, show

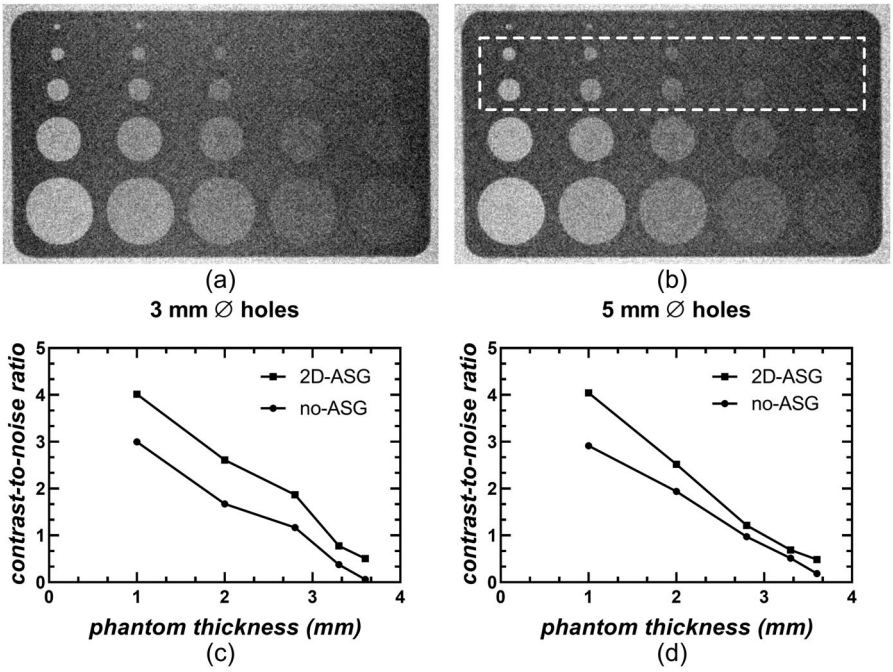

FIGURE 12 Low-contrast object conspicuity: 2D radiographs of the low-contrast phantom acquired with a 15 cm water bath and (a) without ASG, versus (b) with 2D-ASG. (c and d) show improvements in CNR across the 5 and 3 mm holes marked by the dotted box in (b). Images are shown using identical window and level settings.

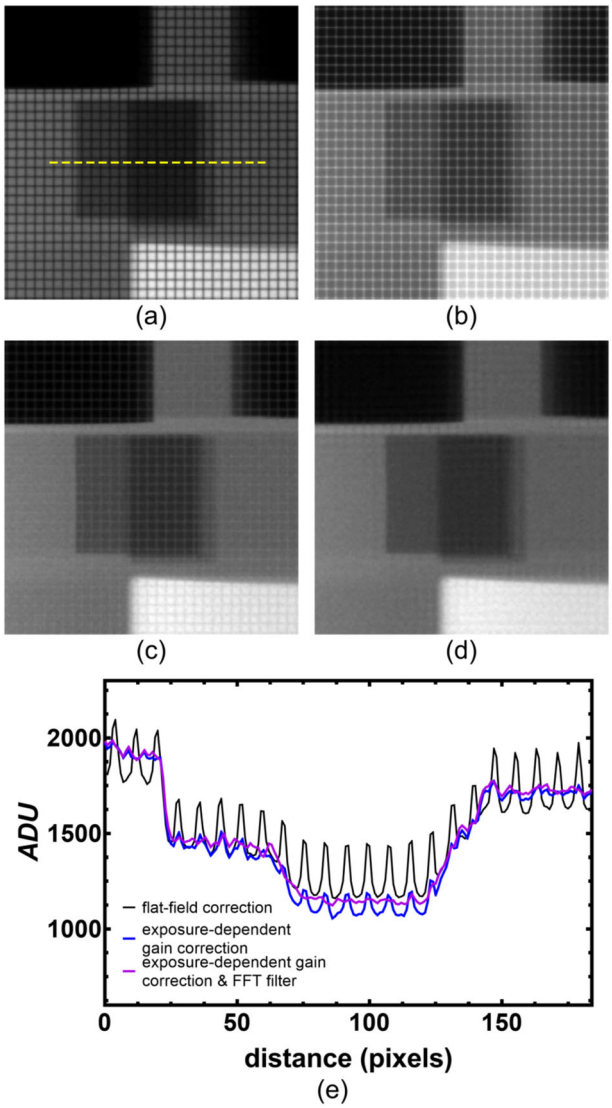

FIGURE 13 Close-up of QA phantom region in a CBCT 2D-projection image. (a) Uncorrected, raw grid-line artifacts (b) with flat-field correction (c) with exposure-dependent gain correction, (d) with exposure-dependent gain correction and notch-FFT-filter and (e) line profiles (across yellow-dotted line in (a)) showing the reduction of grid-line artifact intensity using the exposure-dependent correction method and further notch-FFT-filter

low-HU variations, ~50 HU, after implementation of the proposed methods.

3.5 | CBCT image quality evaluation

3.5.1 | Geometric accuracy and resolution

Figure 16 shows an image of the geometric accuracy plate reconstructed with the 2D-ASG in place. The distance between steel beads was 39.83 ± 0.06 mm compared to the expected 40 ± 0.025 mm, demonstrating excellent in-plane geometric accuracy. Likewise, the out-of-plane distance between tungsten-carbide beads of the first spatial resolution plate of the QA phantom was 14.98 ± 0.07 mm. The interbead distance was designed to be 15 mm.

Spatial resolution was evaluated qualitatively using the bar patterns included in one of the resolution plates of the QA phantom. Figure 17 shows the conservation of spatial resolution with and without the 2D-ASG. Bar patterns for 0.8 line pair/mm (lp/mm) were resolved in both experimental scenarios. These observations were quantitatively verified by the MTF curves calculated using the slanted-edge oriented in the x, y plane (Figure 18). An MTF of 0.1 corresponded to 0.9 lp/mm, which was in agreement with the resolution observed in the bar patterns array. The slight differences between the two MTF curves were attributed to FFT filtering effects in the 2D-ASG scenario.

TABLE 2 Contrast plate CNR calculations with and without 2D-ASG

Bone mineral density (mg.cm^3)	CNR no 2D-ASG	CNR with 2D-ASG
1100	14.4	16.1
400	5.4	6.1
350	5.2	5.6
300	4.7	5.6
250	2.9	3.5
200	2.6	2.9
150	1.5	2.2
100	1	1.2
air	8.3	9.2

3.5.2 | Low contrast and linearity

Table 2 lists the CNR values for bone-mimicking inserts of the contrast plate of the QA phantom in CBCT images with and without 2D-ASG. The arrangement of the inserts and the details of the plate are shown in Figure 19a. The 2D-ASG provided a 9.9% to 48.8% improvement in CNR compared to no 2D-ASG, with a 14.5% average of improvement across inserts. A substantial cupping artifact is visible in the volume acquired without 2D-ASG. This artifact is less conspicuous in the volume acquired with the 2D-ASG.

The second row of Figure 19 shows the calculated CT number (HU) as a function of the bone mineral density of the bone-mimicking inserts located in the contrast plate of the QA phantom. Both volumes presented a significant ($p < 0.0001$) linear correlation between signal intensity and increasing bone density. The differences in mean values and corresponding standard deviations for each insert illustrate the improvements in CNR between the two experimental scenarios.

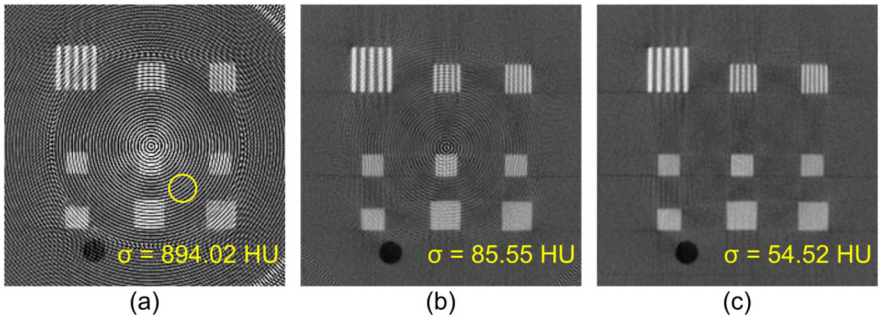

FIGURE 14 Resolution plate of QA phantom reconstructed (a) using linear-gain correction, (b) using exposure-dependent gain correction, and (c) after both exposure-dependent gain correction and Fourier-notch filtering. Standard deviations calculated in the outlined circular, yellow ROI show improvements in image quality using the proposed GLA correction method.

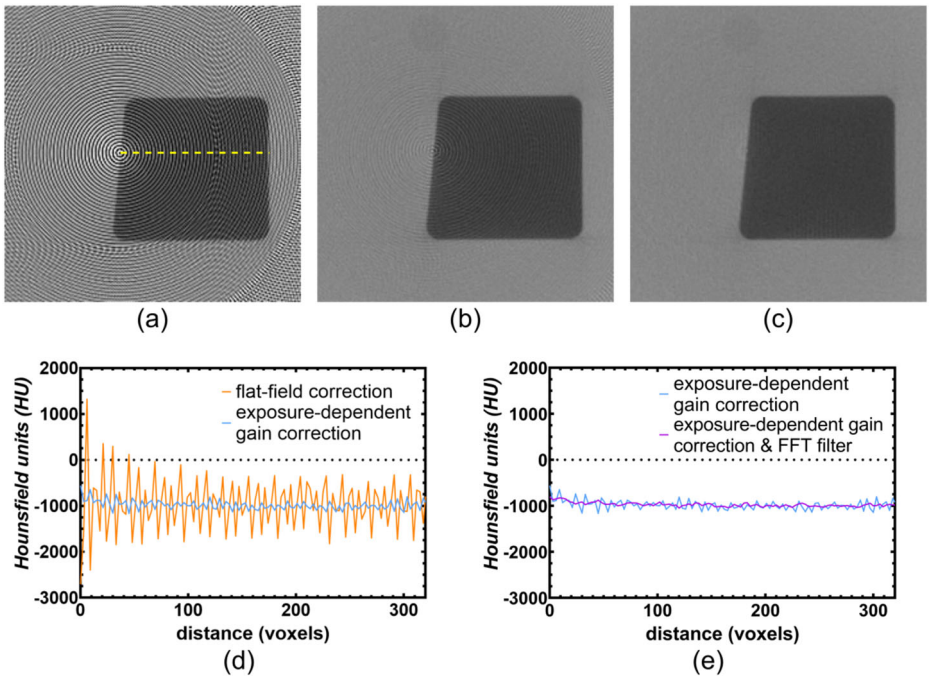

FIGURE 15 CT number accuracy improvements for air-filled, slanted-edge chamber inside the QA phantom. (a) Reconstruction with traditional gain correction (b) with exposure-dependent gain correction, and (c) using Fourier filtering. (d, e) show line profiles, marked by the yellow dotted line in (a), across the air-filled structure.

3.5.3 | Cupping

CBCT reconstructions of the resolution and uniformity plates of the QA phantom without and with the 2D-ASG are shown in Figures 20 and 21. Without the 2D-ASG, HU values were overestimated and contributed to the lower homogeneity of the reconstructions when compared to the data where the 2D-ASG was employed. With the 2D-ASG, shading and cupping artifacts were reduced by 65% of the UI. Residual artifacts were attributed to residual scatter and beam hardening. Modeling the x-ray spectra at 80 kVp with the inherent 1 mm aluminum filtration of the x-ray unit rendered a mean energy of 38.8 keV. The addition of 154 mm of water provided additional filtration that increased the mean energy of the spectrum to 48.18 keV (Figure 22a). Figure 22b shows the decrease in transmission percent of photons at various energies across cobalt–chrome alloy and tungsten.

4 | DISCUSSION

Small-area 2D-ASGs have been previously described as an effective means to prevent scatter-related image quality degradation in CBCT systems.[24,35–37,66] However, the extension to covering a large area of the x-ray detector is not straightforward due to design, fabrication, and implementation considerations.[67] 2D-ASGs have been previously manufactured in tungsten, due

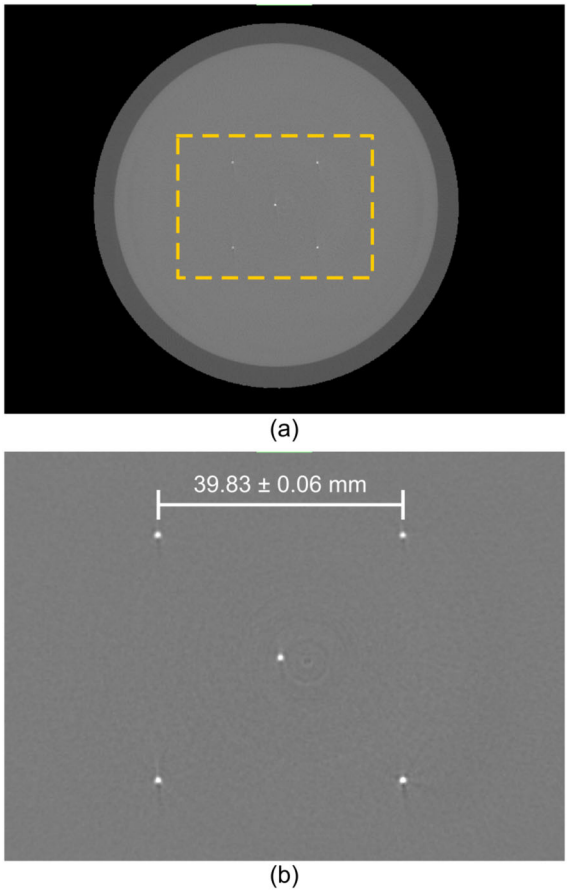

FIGURE 16 (a) CBCT slice of the geometric accuracy plate of the QA phantom and (b) close-up of the area in yellow-dotted lines in (a) showing the five steel beads in the axial plane and measured interbead distance

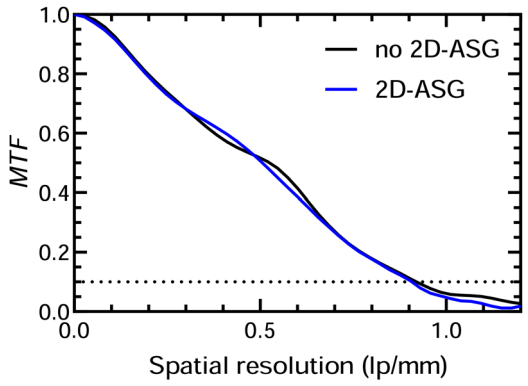

FIGURE 17 Modulation transfer function (MTF) of the CBCT reconstructions measured from the slanted-edge plate of the QA phantom

to its higher attenuation coefficient.[24,35,36] However, our results show that large-area 2D-ASGs manufactured in cobalt–chromium alloy are able to significantly improve image quality for high-scatter scenarios at relatively low diagnostic energies (i.e., 80 kVp). For example, our cobalt–chromium 2D-ASG could then be an effective solution for scatter reduction in peripheral cone-beam CT scanners such as the OnSight 3D Extremity System by Carestream Health.

The design of the large-area grid was achieved using an open-source software utility capable of modeling any grid geometry using a small set of user-defined parameters. This parametric approach addresses the shortcomings of traditional CAD systems, which cannot perform geometric-modeling operations on designs with more than 1000–2000 elements,[52] and allows for the fast and efficient generation of system-specific, grid geometries. The capability to easily model 2D-ASGs with various geometries can be beneficial when running Monte-Carlo simulations or assessing the printability of the design. The flat-panel detector pitch, detector-to-source distance, and size of the 2D-ASG are the most critical aspects to consider. The geometry of the open channels in our parametric software utility has been modified and successfully adapted for other applications involving focused geometries (e.g., gamma collimators).[68]

During printing, the rapid heating and cooling cycles, characteristic of LPBF, can induce high thermal variations that promote residual stresses, warping, cracks, and even complete print failure due to delamination of the part from the build plate.[50,59,69] These residual stresses compound as the part occupies a larger area of the build plate. To the best of our knowledge, the largest 2D-ASG prototypes described in the literature have not exceeded an area of 3×20 cm^2 of the build plate.[24,33,35–37,67] Additionally, the assembling of multiple prototypes into a larger grid presents challenges such as alignment of the assembly and thicker septa at the interface. Our results show that fine-tuning of the print parameters, combined with a cell-by-cell, single-path, scanning strategy, greatly facilitated the fabrication of the large-area 2D-ASGs in cobalt–chrome alloy. We believe that the success of the print was significantly aided by the heat-dissipating nature of the 2D-ASG geometry. The geometry of the grid acted in a similar way to the role of sacrificial supports in LPBF. Sacrificial supports are lattice-based structures used to raise the part from the build plate to dissipate thermal stresses and to facilitate part detachment from the build plate.[70] In the case of 2D-ASGs, the print may fail if the cell size is too large, and therefore, the distance between intersections, or contact points, does not provide enough septal support during fabrication. This is particularly important at the corners of the 2D-ASG where grid septa are most tilted. It is worth mentioning that stress relieving through heat treatment is mandatory to prevent uplifting or deflection of the part after detachment from the build plate.[46,50] Furthermore, the build plate needs to be preheated in order to minimize these effects. The detachment of the part from the build plate must be done carefully and with high accuracy to maintain proper septal alignment relative to the detector

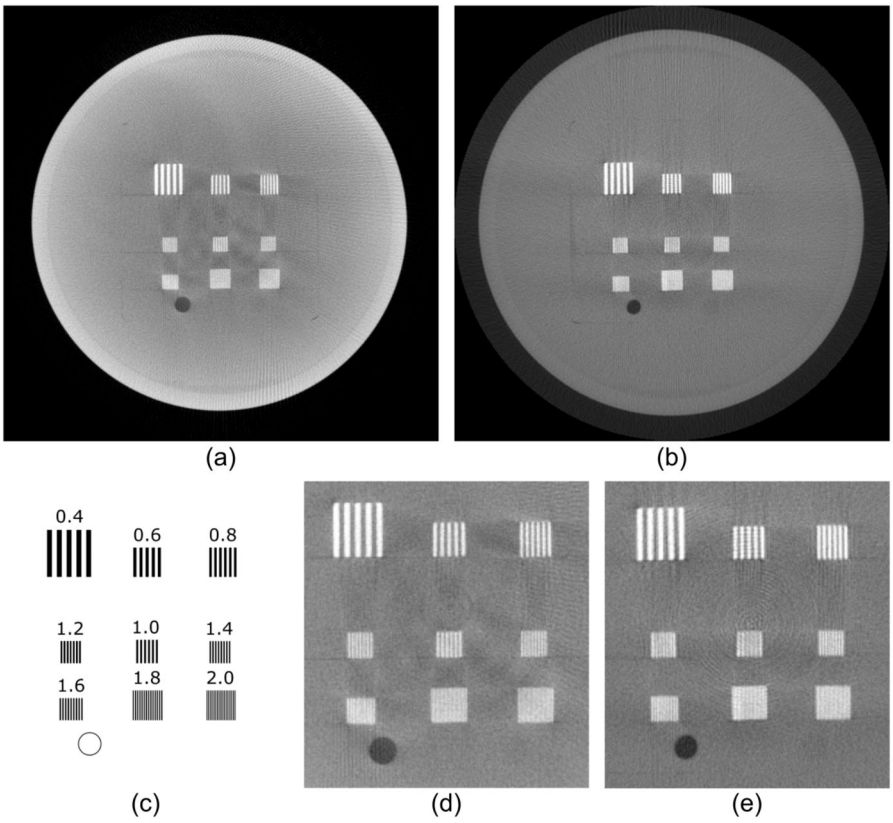

FIGURE 18 Qualitative evaluation of spatial resolution using the resolution plate of the QA phantom. (a) CBCT reconstruction without 2D-ASG. (b) CBCT reconstruction with 2D-ASG. (c) Details of the resolution plate with interleaved Mylar and Aluminum sheets in lp/mm. (d, e) magnified images of (a) and (b), respectively.

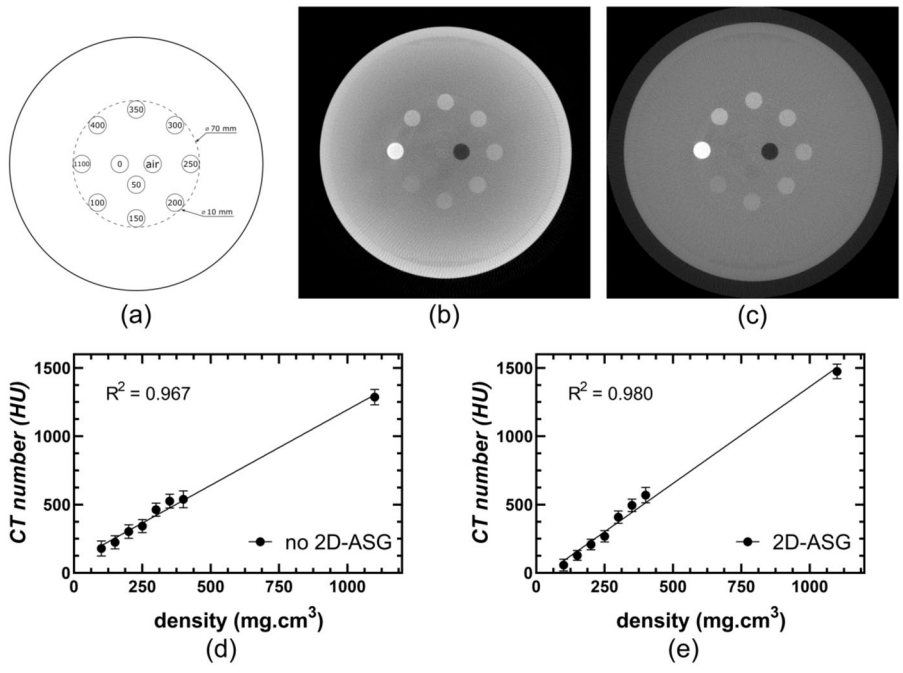

FIGURE 19 Evaluation of contrast and linearity using the contrast plate of the QA phantom. (a) Details of the contrast plate showing BMD inserts at various densities. (b) CBCT reconstruction without 2D-ASG. (c) CBCT reconstruction with 2D-ASG. (d) Linearity plots for the reconstruction without the 2D-ASG (d), and with the 2D-ASG (e) (linearity plots represent HU as a function of bone mineral density)

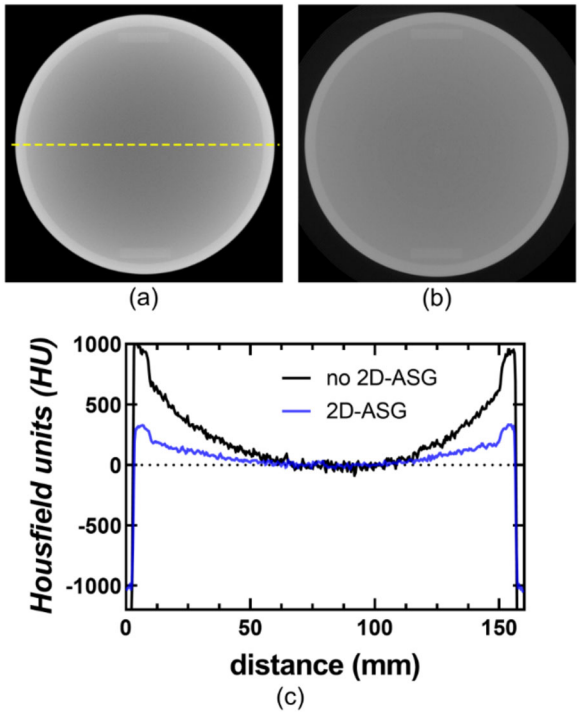

FIGURE 20 CT number accuracy evaluation using the uniformity plate of the QA phantom (a) CBCT reconstruction of the uniformity plate without 2D-ASG. (b) CBCT reconstruction of the uniformity plate with 2D-ASG. (c) HU profile along the dotted line in (a)

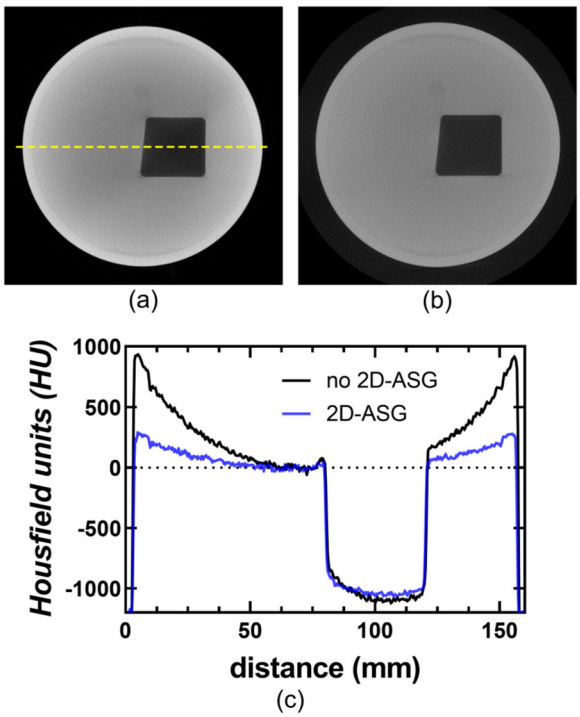

FIGURE 21 CT number accuracy evaluation using the slanted-edge, MTF, resolution plate of the QA phantom (a) CBCT reconstruction of the resolution plate without the 2D-ASG. (b) CBCT reconstruction of the resolution plate with the 2D-ASG. (c) shows a linear profile in HU across the phantom along the yellow dotted line in (a).

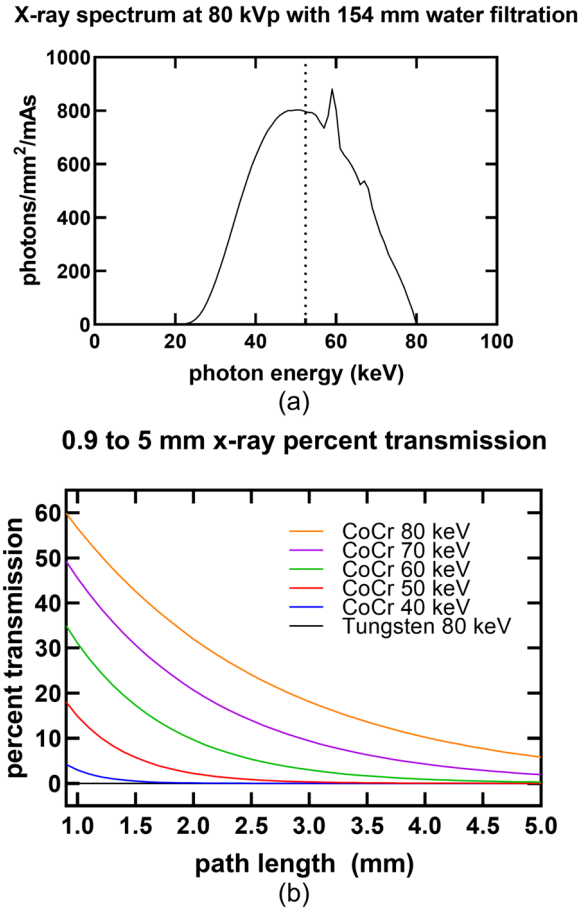

FIGURE 22 Experimental x-ray spectral characteristics and percent transmission through 2D-ASG septa. (a) Characterization of the x-ray spectrum for CBCT data acquisition with an additional 154 mm of water filtration. (b) Photon percent transmission through 0.9–5 mm of cobalt–chrome septal material

face. Access to specialized machining (e.g., wire-EDM) should be considered.

It is desirable to print grid septa as thin as possible because it reduces the effects of GLA and maximizes the primary transmission of the grid. Grid septal thickness is determined by laser energy, scanning strategy, powder particle size, and laser spot size. Our parameters included a spot size that was 2–5 bigger than powder particles. Similar to other researchers, our nominal thickness limit was around 100 μm. Grid septa thickness could theoretically be reduced with powders that have smaller particle size and LPBF machines with smaller focal spot. Although our results showed that a single-path strategy was effective at producing structurally stable septa, this may not be the case for other metals or alloys. Xie et al.[71] have shown that a double-path strategy improves both wall thickness and density for similar objects printed using tungsten. Our design matched the primary transmission characteristics of other prototypes in the literature; however, the pitch of our 2D-ASG made GLA correction challenging. Increasing both grid pitch

and ratio may be an effective alternative for design optimization.

The choice of a 2D-ASG material with an electron density as high as possible will maximize the scatter rejection efficiency of the grid. However, consideration of material properties such as strength, rigidity, brittleness, and thermal conductivity, as well as cost and toxicity should be taken into account. At the time of these experiments, the LPBF printers that were capable of printing a grid this large and were available at our AM facility could routinely print only in titanium and cobalt–chrome alloys. In our facilities, the extension to printing in other denser metals, such as tungsten, is not trivial for a variety of practical reasons, including cross contamination of various metal powders, and contraventions of ISO certifications. Nevertheless, in the future, we could certainly reproduce our work in tungsten for applications where only tungsten will suffice. In which case, it will be necessary to refine printing parameters such as exposure time, laser energy, and scanning strategy.

In our cobalt–chrome design, all photons with an angle of incidence less than 84.28° degrees will begin to be filtered by the grid septa based on the calculation $tan(ø) = grid\text{-}height/cell\text{-}width$. Photons at the mean energy of our spectrum travelling through a 154-mm water-filled phantom (52.4 keV) are 50% filtered by a minimum of 0.914 mm of path length through the cobalt–chrome septa with an angle of incidence of 83.7°. However, photons at the peak energy of our spectrum (80 keV) are only 40% filtered at the same angle of incidence. Figure 22b shows the percent transmission for 80, 70, 60, 50, and 40 keV photons through various path lengths in cobalt–chrome, and 80 keV through tungsten, as well as the modeled spectrum for our experiments. The inability of our grid to completely remove scattered photons over 52.4 keV was a limitation; however, our results suggest that scatter was sufficiently reduced to improve image quality. Future work includes the printing of similar sized 2D-ASG using tungsten and a smaller 2D-ASG on a different 3D printer with a smaller build plate (AM-125; Renishaw plc, New Mills Wotton-under-Edge, UK), on which tungsten has already been implemented.

Grid-line artifacts are a major concern when it comes to the implementation of 2D-ASG.[49] If septal thickness is larger than the detector elements, fixed-pattern noise correction might not be feasible, leading to severe ring artifacts in the CBCT reconstruction. In our implementation, no detector element received less than 30% of primary signal. Furthermore, consistent grid structure was observed across the whole 2D-ASG. This demonstrates the accurate geometry of focused septa. Our combination of exposure-dependent gain correction and FFT notch filtering allowed for the effective correction of grid-line artifacts. We believe that the residual GLA after exposure-dependent gain correction were caused by a combination of residual scatter, temporal blurring due to ghosting, and nonlinear veiling glare. Other groups have presented alternative methods to correct GLA, including total variation suppression and residual scatter characterization.[33,37] Our results show that exposure-dependent gain correction outperforms traditional flat-field corrections and might reduce the need for alternative methods in other 2D-ASG geometries, especially if the 2D-ASG has a larger pitch and improved scatter rejection characteristics (e.g., made up of tungsten). Our GLA correction method will require testing for the case of clinical CBCT systems due to the effect of gantry flexure and potential grid misalignment as a function of angle. In this scenario, the location of the x-ray focal spot might change, impacting the accuracy of the gain maps. An angle-dependent calibration may be required to maintain optimal GLA correction. Although the FFT notch filter was able to remove GLA in the center of the field-of-view, some artifacts were noticeable near the edges of the 2D-ASG frame. These artifacts were caused by Gibbs ringing and affected the periphery of the CBCT reconstruction. This could be a limitation in the case of volume stitching.

Similar to other studies,[24,35–37] improvements in image quality using our 2D-ASG were particularly noticeable in CT number accuracy and low-contrast visualization, 65% and 48% improvement, respectively. Although our results do not match the level of improvement reported by these studies, we believe that there are significant differences in our experimental setup that account for these discrepancies. First, it is possible that the residual cupping observed in our images could be caused by residual scatter not captured by our cobalt–chrome 2D-ASG. Second, our experiments covered a larger area of the flat-panel detector, were conducted at lower energies (80 vs. 125 kVp), and did not include additional filtration to ameliorate the effects of beam hardening. Finally, our volumes were reconstructed using a limited number of projection images (215° vs. 360°). We plan to use iterative reconstruction methods in the future to reduce streak artifacts that are characteristic of Parker-weighted CBCT reconstructions.

5 | CONCLUSION

We have successfully designed, manufactured, and implemented a first large-area, 2D-ASG for flat-panel CBCT. Traditional CAD design techniques for these complicated structures are unwieldy, inefficient, and do not lend themselves well to design revision. Our implementation of an open-source, parametric modeling approach significantly reduces the design time, computational burden, and greatly facilitates revisions and design changes.

We optimized the AM process to successfully produce the required grid geometry ensuring mechanical stability, scatter rejection, and optimal primary transmission. These optimizations included considerations for

the energy deposition within the melt pool, as well as the implementation of a cell-by-cell single-path scanning strategy. Grid septa thickness and transmission characteristics of the 2D-ASG were rigorously evaluated using a metrology microscope and an automated script to average septa thickness with subpixel resolution.

Grid line artifacts (GLAs) were corrected using both an exposure-dependent gain correction and an FFT notch filter. The relatively high pitch of our 2D-ASG compared to previously reported ASG prototypes exacerbated the GLA-removal problem, which warrants further investigation using iterative methods or artificial intelligence (AI).

Significant improvements (65%) in CT number accuracy, as measured by the UI, were observed when using the 2D-ASG, making these CBCT reconstructions more suitable for quantitative imaging tasks and for clinical scenarios that require accurate image segmentation. Significant CNR improvements were observed for low-contrast bone-mineral inserts. These improvements in CNR could be key when diagnosing low-contrast pathologies in clinical imaging. The use of a 2D anti-scatter grid also separates the effect of scatter from beam-hardening, making it potentially easier to correct remaining beam-hardening artifacts using established methods.[72]

Future work includes the implementation of the 2D-ASG in a clinical CT system and at higher energies. In these systems, an angle-dependent gain correction may be required to reduce the effects of gantry flexure. Iterative or AI-based reconstruction techniques could also be used to improve GLA correction and the noise characteristics of our CBCT reconstructions. We anticipate that, at higher energies, 2D-ASGs manufactured in cobalt–chrome might not be as effective as those printed in other more attenuating metals, such as tungsten.

ACKNOWLEDGMENTS

Support for this project came from the Canadian Institutes of Health Research (Foundation Grant FDN 148474) and the Ontario Research Fund (Research Excellence RE-077-66). D.W.H. is the Dr. Sandy Kirkley Chair in Musculoskeletal Research within the Schulich School of Medicine & Dentistry at Western University. S.F.C. is supported in part by a Transdisciplinary Bone & Joint Training Award from the Collaborative Training Program in Musculoskeletal Health Research at The University of Western Ontario. The authors would also like to thank Matt Parkes and Tom Chmiel at ADEISS for their assistance with the manufacturing of the 2D-ASG.

CONFLICTS OF INTEREST

The authors have no conflicts to disclose.

DATA AVAILABILITY STATEMENT

The data that support the findings of this study are available from the corresponding author upon reasonable request.

ORCID

Santiago Fabian Cobos
https://orcid.org/0000-0002-7239-3240
Christopher James Norley
https://orcid.org/0000-0001-8891-3434
David Wayne Holdsworth
https://orcid.org/0000-0002-0603-5322

REFERENCES

1. Jaffray D, Siewerdsen J. Cone-beam computed tomography with a flat-panel imager: initial performance characterization. *Med Phys*. 2000;27(6):1311-1323.
2. Jaffray DA, Siewerdsen JH, Wong JW, Martinez AA. Flat-panel cone-beam computed tomography for image-guided radiation therapy. *Int J Radiat Oncol Biol Phys*. 2002;53(5):1337-1349.
3. Fahrig R, Moreau M, Holdsworth D. Three-dimensional computed tomographic reconstruction using a C-arm mounted XRII: correction of image intensifier distortion. *Med Phys*. 1997;24(7):1097-1106.
4. Manzke R, Grass M, Hawkes D. Artifact analysis and reconstruction improvement in helical cardiac cone beam CT. *IEEE Trans Med Imaging*. 2004;23(9):1150-1164.
5. Sonke JJ, Zijp L, Remeijer P, van Herk M. Respiratory correlated cone beam CT. *Med Phys*. 2005;32(4):1176-1186.
6. Nemtoi A, Czink C, Haba D, Gahleitner A. Cone beam CT: a current overview of devices. *Dentomaxillofacial Radiol*. 2013;42(8):20120443.
7. Yegya-Raman N, Kim S, Deek MP, et al. Daily image guidance with cone beam computed tomography may reduce radiation pneumonitis in unresectable non-small cell lung cancer. *Int J Radiat Oncol Biol Phys*. 2018;101(5):1104-1112.
8. Lechuga L, Weidlich GA. Cone beam CT vs. fan beam CT: a comparison of image quality and dose delivered between two differing CT imaging modalities. *Cureus*. 2016;8(9).
9. Elstrøm UV, Muren LP, Petersen JB, Grau C. Evaluation of image quality for different kV cone-beam CT acquisition and reconstruction methods in the head and neck region. *Acta Oncol (Madr)*. 2011;50(6):908-917.
10. Zhu L, Xie Y, Wang J, Xing L. Scatter correction for cone-beam CT in radiation therapy. *Med Phys*. 2009;36(6Part1):2258-2268.
11. Nagarajappa AK, Dwivedi N, Tiwari R. Artifacts: the downturn of CBCT image. *J Int Soc Prevent Community Dentistry*. 2015;5(6):440.
12. Siewerdsen JH, Jaffray DA. Cone-beam computed tomography with a flat-panel imager: magnitude and effects of x-ray scatter. *Med Phys*. 2001;28(2):220-231.
13. Pauwels R, Araki K, Siewerdsen J, Thongvigitmanee SS. Technical aspects of dental CBCT: state of the art. *Dentomaxillofacial Radiol*. 2014;44(1):20140224.
14. Pauwels R, Jacobs R, Singer SR, Mupparapu M. CBCT-based bone quality assessment: are Hounsfield units applicable? *Dentomaxillofacial Radiol*. 2014;44(1):20140238.
15. Nackaerts O, Maes F, Yan H, Souza PC, Pauwels R, Jacobs R. Analysis of intensity variability in multislice and cone beam computed tomography. *Clin Oral Implants Res*. 2011;22(8):873-879.
16. Bhoosreddy AR, Sakhavalkar PU. Image deteriorating factors in cone beam computed tomography, their classification, and measures to reduce them: a pictorial essay. *J Indian Acad Oral Med Radiol*. 2014;26(3):293.
17. Mao W, Gardner SJ, Snyder KC, et al. On the improvement of CBCT image quality for soft tissue-based SRS localization. *J Appl Clin Med Phys*. 2018;19(6):177-184.
18. Gardner SJ, Studenski MT, Giaddui T, et al. Investigation into image quality and dose for different patient geometries with multiple cone-beam CT systems. *Med Phys*. 2014;41(3).
19. Cha BK, Jeon S, Seo C-W, et al. Optimization of X-ray image acquisition and reconstruction for a C-arm CBCT

system with a flat-panel detector. *Nucl Instrum Methods Phys Res A*. 2018;924:343.
20. Posiewnik M, Piotrowski T. A review of cone-beam CT applications for adaptive radiotherapy of prostate cancer. *Physica Med*. 2019;59:13-21.
21. Hansen DC, Landry G, Kamp F, et al. ScatterNet: a convolutional neural network for cone-beam CT intensity correction. *Med Phys*. 2018;45(11):4916-4926.
22. Shi L, Wang AS, Wei J, Zhu L. Fast shading correction for cone-beam CT via partitioned tissue classification. *Phys Med Biol*. 2019.
23. Pellerin O, Pereira H, Ty CVN, et al. Is dual-phase C-arm CBCT sufficiently accurate for the diagnosis of colorectal cancer liver metastasis during liver intra-arterial treatment? *Eur Radiol*. 2019:1-11.
24. Altunbas C, Kavanagh B, Alexeev T, Miften M. Transmission characteristics of a two dimensional antiscatter grid prototype for CBCT. *Med Phys*. 2017;44(8):11.
25. Zhao W, Vernekohl D, Zhu J, Wang L, Xing L. A model-based scatter artifacts correction for cone beam CT. *Med Phys*. 2016;43(4):1736-1753.
26. Stankovic U, Ploeger LS, van Herk M, Sonke JJ. Optimal combination of anti-scatter grids and software correction for CBCT imaging. *Med Phys*. 2017;44(9):4437-4451.
27. Rührnschopf EP, Klingenbeck K. A general framework and review of scatter correction methods in x-ray cone-beam computerized tomography. Part 1: scatter compensation approaches. *Med Phys*. 2011;38(7):4296-4311.
28. Rührnschopf and EP, Klingenbeck K. A general framework and review of scatter correction methods in cone beam CT. Part 2: scatter estimation approaches. *Med Phys*. 2011;38(9):5186-5199.
29. Maier J, Eulig E, Vöth T, et al. Real-time scatter estimation for medical CT using the deep scatter estimation: method and robustness analysis with respect to different anatomies, dose levels, tube voltages, and data truncation. *Med Phys*. 2019;46(1):238-249.
30. Altunbas C, Park Y, Yu Z, Gopal A. A unified scatter rejection and correction method for cone beam computed tomography. *Med Phys*. 2021;48(3):1211-1225.
31. Siewerdsen JH, Moseley D, Bakhtiar B, Richard S, Jaffray DA. The influence of antiscatter grids on soft-tissue detectability in cone-beam computed tomography with flat-panel detectors. *Med Phys*. 2004;31(12):3506-3520.
32. Wiegert J, Bertram M, Schaefer D, et al. Performance of standard fluoroscopy antiscatter grids in flat-detector-based cone-beam CT. *Paper presented at Medical Imaging 2004: Physics of Medical Imaging*. 2004.
33. Alexeev T, Kavanagh B, Miften M, Altunbas C. Novel ring artifact suppression method for CBCT imaging with two-dimensional antiscatter grids. *Med Phys*. 2019;46:2181.
34. Schafer SW, Stayman J, Zbijewski W, Schmidgunst C, Kleinszig GH. Siewerdsen J. Antiscatter grids in mobile C-arm cone-beam CT: effect on image quality and dose. *Med Phys*. 2012;39(1):153-159.
35. Alexeev T, Kavanagh B, Miften M, Altunbas C. Two-dimensional antiscatter grid: a novel scatter rejection device for cone-beam computed tomography. *Med Phys*. 2018;45(2):529-534.
36. Park Y, Alexeev T, Miller B, Miften M, Altunbas C. Evaluation of scatter rejection and correction performance of 2D antiscatter grids in cone beam computed tomography [published online ahead of print 2021/02/09]. *Med Phys*. 2021;48(4):1846-1858.
37. Yu Z, Park Y, Altunbas C. Simultaneous scatter rejection and correction method using 2D antiscatter grids for CBCT [published online ahead of print 2020/04/22]. *Proc SPIE Int Soc Opt Eng*. 2020;11312.
38. Vogtmeier G, Dorscheid R, Engel KJ, et al. Two-dimensional anti-scatter grids for computed tomography detectors. Paper presented at Medical Imaging 2008: Physics of Medical Imaging. 2008.
39. Tang C-M, Stier E, Fischer K, Guckel H. Anti-scattering X-ray grid. *Microsyst Technol*. 1998;4(4):187-192.
40. Lee S, Chung W. Quantitative analysis of effects of the grid specifications on the quality of digital radiography images. *Australas Phys Eng Sci Med*. 2019;42(2):553-561.
41. Veldkamp WJ, Thijssen MA, Karssemeijer N. The value of scatter removal by a grid in full field digital mammography. *Med Phys*. 2003;30(7):1712-1718.
42. Lehmann V, Rönnebeck S. MEMS techniques applied to the fabrication of anti-scatter grids for X-ray imaging. *Sens Actuators, A*. 2002;95(2-3):202-207.
43. Goldenberg B, Lemzyakov A, Nazmov V, Palchikov E. LIGA method of forming high-contrast collimators and anti-scatter grids with high aspect ratio. *Resource-Efficient Technol*. 2018;(2):1-4.
44. Grasso M, Colosimo BM. Process defects and in situ monitoring methods in metal powder bed fusion: a review. *Meas Sci Technol*. 2017;28(4):044005.
45. Kretzschmar N, Ituarte IF, Partanen J. A decision support system for the validation of metal powder bed-based additive manufacturing applications. *Int J Adv Manufacturing Technol*. 2018;96(9-12):3679-3690.
46. Sun S, Brandt M, Easton M. Powder bed fusion processes: An overview. In: *Laser Additive Manufacturing*. Elsevier; 2017:55-77.
47. Wu H, Li J, Wang H. Removing ring artifacts in cone-beam CT via TV-stokes and unidirectional total variation model. *Med Phys*. 2019;46(4):1719-1727.
48. Altunbas C, Lai CJ, Zhong Y, Shaw CC. Reduction of ring artifacts in CBCT: detection and correction of pixel gain variations in flat panel detectors. *Med Phys*. 2014;41(9).
49. Jacobs JWM, Inventor; Koninklijke Philips NV, assignee. X-ray anti scatter grid. 03-24-2021, 2021.
50. Bartlett JL, Li X. An overview of residual stresses in metal powder bed fusion. *Additive Manufact*. 2019;27:131-149.
51. Wang C-S, Chang T-R, Hu Y-N, Hsiao C-Y, Teng C-K. STL mesh re-triangulation in rapid prototyping manufacturing. Paper presented at IEEE International Conference on Mechatronics. 2005. ICM'05. 2005.
52. Gibson I, Rosen D, Stucker B, Khorasani M. Design for additive manufacturing. In: *Additive Manufacturing Technologies*. Springer; 2021:555-607.
53. Ghouse S, Babu S, Van Arkel RJ, Nai K, Hooper PA, Jeffers JR. The influence of laser parameters and scanning strategies on the mechanical properties of a stochastic porous material. *Mater Des*. 2017;131:498-508.
54. Ciurana J, Hernandez L, Delgado J. Energy density analysis on single tracks formed by selective laser melting with CoCrMo powder material. *Int J Adv Manufact Technol*. 2013;68(5-8):1103-1110.
55. Isaza J, Aumund-Kopp C, Wieland S, Petzoldt F, Bauschulte M, Fraunhofer DG. AM-special processes and materials: new materials and applications by 3D-printing for innovative approaches. Paper presented at European Congress and Exhibition on Powder Metallurgy. European PM Conference Proceedings. 2015.
56. Hubbell JH, Seltzer SM. Tables of X-ray mass attenuation coefficients and mass energy-absorption coefficients 1 keV to 20 MeV for elements Z = 1 to 92 and 48 additional substances of dosimetric interest. National Institute of Standards and Technology-PL; 1995.
57. Guo M, Gu D, Xi L, Du L, Zhang H, Zhang J. Formation of scanning tracks during selective laser melting (SLM) of pure tungsten powder: Morphology, geometric features and forming mechanisms. *Int J Refract Met Hard Mater*. 2019;79:37-46.
58. Mingear J, Zhang B, Hartl D, Elwany A. Effect of process parameters and electropolishing on the surface roughness

of interior channels in additively manufactured nickel-titanium shape memory alloy actuators. *Additive Manuf*. 2019;27:565-575.
59. Yang Y, Jamshidinia M, Boulware P, Kelly S. Prediction of microstructure, residual stress, and deformation in laser powder bed fusion process. *Comput Mech*. 2018;61(5):599-615.
60. Baronette R. Quantitative analysis of three-dimensional cone-beam computed tomography using image quality phantoms. [Masters dissertation]. London, Western University; 2018.
61. Cobos SF, Nikolov HN, Pollmann SI, Holdsworth DW. Reduction of ring artifacts caused by 2D anti-scatter grids in flat-panel CBCT. Paper presented at *Medical Imaging 2020: Physics of Medical Imaging. 2020*.
62. Chakraborty D, Tarafder MK, Banerjee A, Chaudhuri SB. Gabor-based spectral domain automated notch-reject filter for quasi-periodic noise reduction from digital images. *Multimedia Tools Appl*. 2019;78(2):1757-1783.
63. Fokas G, Vaughn VM, Scarfe WC, Bornstein MM. Accuracy of linear measurements on CBCT images related to presurgical implant treatment planning: a systematic review. *Clin Oral Implants Res*. 2018;29:393-415.
64. Du LY, Umoh J, Nikolov HN, Pollmann SI, Lee T-Y, Holdsworth DW. A quality assurance phantom for the performance evaluation of volumetric micro-CT systems. *Phys Med Biol*. 2007;52(23):7087.
65. Petrov IE, Nikolov HN, Holdsworth DW, Drangova M. Image performance evaluation of a 3D surgical imaging platform. Paper presented at Medical Imaging 2011: *Physics of Medical* Imaging. 2011.
66. Altunbas C. A hybrid flat panel detector for cone beam ct systems. *Google Patents*; 2018.
67. Altunbas C, Alexeev T, Miften M, Kavanagh B. Effect of grid geometry on the transmission properties of 2D grids for flat detectors in CBCT. *Phys Med Biol*. 2019;64(22):225006.
68. Sydney LM, Wilson SP, Nikolov HN, Stodilka R, Holdsworth DW. Highly focused collimators for increased resolution of hand-held gamma probes. Paper presented at Imaging Network Ontario Symposium; March 23–24, 2021.
69. Mercelis P, Kruth JP. Residual stresses in selective laser sintering and selective laser melting. *Rapid Prototyping J*. 2006;12:254.
70. Hussein A, Hao L, Yan C, Everson R, Young P. Advanced lattice support structures for metal additive manufacturing. *J Mater Process Technol*. 2013;213(7):1019-1026.
71. Xie Y-j, Yang H-c, Wang X-b, Zhao L, Kuang C-j, Han W. Control of wall thickness and surface morphology of tungsten thin wall parts by adjusting selective laser melting parameters. *J Iron Steel Res Int*. 2019;26(2):182-190.
72. Edey D, Pollmann S, Lorusso D, Drangova M, Flemming R, Holdsworth D. Extending the dynamic range of biomedical micro-computed tomography for application to geomaterials. *J X Ray Sci Technol*. 2019;27(5):919-934.

SUPPORTING INFORMATION

Additional supporting information can be found online in the Supporting Information section at the end of this article.

How to cite this article: Cobos SF, Norley CJ, Nikolov HN, Holdsworth DW. 3D-printed large-area focused grid for scatter reduction in cone-beam CT. *Med Phys*. 2023;50:240–258. https://doi.org/10.1002/mp.16005